Magnetoimpedance of Epitaxial Y3Fe5012 (001) Thin Film in Low-Frequency Regime

doi: https://doi.org/10.1021/acsami.0c13213

Magnetoimpedance in epitaxial $Y_3Fe_5O_{12}$ (001) thin film in low-frequency regime

Rohit Medwal[1§], Ushnish Chaudhuri[2§], Joseph Vimal Vas[1], Angshuman Deka[3], Surbhi Gupta[3*], Martial Duchamp[4], Hironori Asada[5], Yasuhiro Fukuma[3], Mahendiran Ramanathan[2,] and Rajdeep Singh Rawat[1*]

1. Natural Science and Science Education, National Institute of Education, Nanyang Technological University, 637616, Singapore
2. Physics Department, National University of Singapore, Republic of Singapore 117551
3. Graduate of Computer Science and Electronics, Kyushu Institute of Technology, 680-4 Kawazu, Iizuka 820-8502, Japan
4. School of Material Science and Engineering, Facility for Analysis, Characterization, Testing and Simulation (FACTS), Nanyang Technological University, Singapore
5. Graduate School of Sciences and Technology for Innovation, Yamaguchi University, Ube 755-8611, Japan

§ Equal contribution

Abstract: The atomically flat interface of $Y_3Fe_5O_{12}$ (YIG) thin film and $Gd_3Ga_5O_{12}$ (GGG) substrate play a vital role in obtaining the magnetization dynamics of YIG below and above the anisotropy field. Here, magneto-impedance (MI) is used to investigate the magnetization dynamics in fully epitaxial 45 nm YIG thin films grown on the GGG (001) substrates using a copper strip coil in the MHz-GHz frequency region. The resistance (R) and reactance (X), which are components of impedance (Z), allow us to probe the absorptive and dispersive components of the dynamic permeability, whereas a conventional spectrometer only measures the field derivative of the power absorbed. The distinct excitation modes arising from the uniform and non-uniform excitation of magnetization dynamics of the magnetization vector of YIG, above and below the anisotropy field, are observed. The magneto-dynamics clearly shows the visible dichotomy between two resonant fields below and above the anisotropy field and its motion as a function of the direction of the applied magnetic field. A low value of the damping factor $\sim 4.7 - 6.1 \times 10^{-4}$ is estimated for uniform excitation mode with anisotropy field of 65 ± 2 Oe. Investigation of anisotropy field dependent magneto-dynamics across these two different regimes, below and above anisotropy field, in the low-frequency mode can be used in designing the YIG based resonators, oscillators, filters, and magnonic devices.

Keywords: Magnetization dynamics, magneto-impedance, YIG, anisotropy field

*Correspondence: rajdeep.rawat@nie.edu.sg, surbhi.gupta208@gmail.com

I. Introduction

Yttrium iron garnet (YIG, $Y_3Fe_5O_{12}$), is a well-known ferrimagnetic insulator with low damping of $\sim 10^{-5}$ and is among prevalent choices to study spin current related transport phenomena such as spin Seebeck effect, spin Hall magnetoresistance, spin-orbit magnetoresistance, spin pumping, and spin pumping - inverse spin Hall effect measurements, etc[1-7]. The low Gilbert damping factor of YIG allows the transfer of the spin information over a longer distance without unwanted spurious effects otherwise observed in metallic ferromagnets[1, 3, 7-9]. Further, structural quality of the YIG thin film and its magnetic properties such as effective magnetization, gyromagnetic ratio, anisotropy fields, and magnon-magnon interaction also play crucial role in realizing spin transport across YIG and its heterointerfaces with heavy metals[10]. Where, a comprehensive investigation of magnetization dynamics of YIG, below and above the anisotropy field, is advantageous to gain detail insight and determine unambiguously its magnetic properties[11-12]. The conventional technique employed to study the magnetization dynamics and to estimate the aforementioned magnetic parameters is the ferromagnetic resonance (FMR)[13]. In FMR measurements, usually, the high-frequency magnetization dynamics are excited by applying magnetic field higher than that of the anisotropy field of the magnetic material exhibiting the single domain behaviour[13]. The low-frequency magnetization dynamics excited below the anisotropy field of material, are very sensitive to magnetic interactions and therefore require careful study[13-14]. In particular, a clean and atomically defined interface of the $Gd_3Ga_5O_{12}$ (GGG) and YIG with minimum lattice distortion is also a prerequisite to excite magneto-dynamics below the anisotropy field of YIG[10-11]. Further, the alternative approach of magneto-impedance (MI) measurement technique is recently used for the low-frequency magnetization dynamics and to characterize the different magnetic properties of various thin film materials[15-19]. The MI technique measures the changes in complex impedance ($Z = R + jX$) of magnetic materials placed under the

external applied magnetic field (H), where $R \propto \omega\mu_0\mu_r''$ is the oscillating resistance, $X \propto \omega\mu_0\mu_r'$ is the reactance, ω is the frequency of the rf signal, μ_0 and μ_r defines the permeability of free space and relative permeability of the material. The relative permeability $\mu_r = \mu_r' - j\mu_r''$ induces changes in impedance due to the changes in the absorptive component (μ_r'') as well as changes in the dispersive component (μ_r') of the permeability[15-17]. The information regarding the dispersion and absorption enables an unprecedented understanding of in-plane magnetic anisotropy and magnetic interactions in different crystallographic directions in the material under investigation.

In the present paper, we employed the MI measurements to record the change in the impedance $Z\ (\omega, M)$ of YIG as a function of frequency and the orientation of the magnetization M in high-quality epitaxial YIG(001) film making an atomically flat interface with bottom GGG(001) substrate. The experimentally obtained MI data perpetually exhibits the dependence of the impedance, and thereby magnetization dynamics, of YIG on applied rf frequency and subsequently different magnetic properties including effective magnetization, gyromagnetic ratio, anisotropy field and the damping factor of epitaxial YIG thin film are characterized. The low-frequency magnetization dynamics enables the direct estimation the anisotropy field of the YIG thin film as well as the relative angle of local magnetization with applied magnetic field. Thus, the MI measurements provide an additional way to accurately investigate the magnetic properties and order parameters of the YIG material in low-frequency regime suitable for various applications such as resonators and microwave filters.

II. Experimental Section

Epitaxial YIG (001) thin film with thickness ~ 45 nm was grown on the GGG substrate with (001) orientation using high-vacuum rf sputtering. Before deposition, the substrates were rinsed with acetone and precleaned with ethanol using sonication for 5 minutes. Thereafter, the room temperature deposition was carried out in partial oxygen pressure to maintain the oxygen

stoichiometry. The rf power during the YIG deposition was kept at 100 Watt. The deposited YIG thin film was then subjected to optimized thermal annealing at 750 °C for 4 hours with the ramp rate of 8 °C/minute under the ambient atmospheric conditions, followed by the cooling up to 400 °C at a rate of 1 °C/minute. After 400 °C, the sample was allowed to cool naturally to room temperature. To examine the epitaxial growth of YIG (001) thin film and interface roughness, the X-ray diffraction (XRD) and X-ray reflectivity (XRR) measurement was performed by Bruker D8 Discover using Cu K_α x-ray source. High resolution transmission electron microscopy (TEM) measurements were conducted using a JEOL Grand ARM300 with a cold FEG gun at 300 kV. The cross-sectional sample for the TEM studies was prepared using a Focused Ion Beam (FIB) milling[20]. The lamella fabrication was done using a Zeiss Crossbeam 540 FIB equipped with a dual gun and an *in-situ* micromanipulator for transferring the cross-section sample to the TEM half-grid. MI measurements were performed using an Agilent E4991A impedance analyzer. Room temperature M-H hysteresis loops were traced using vibrating sample magnetometer. Next, an indirect approach to measure the impedance while sweeping the DC magnetic field (H_{dc}) for a given rf frequency (to provide oscillating magnetic field, H_{rf}) varied from 500-2000 MHz range is utilized[17]. The sample size of 3 mm × 3 mm was placed in between the copper coil which affects the magnetic flux distribution and thereby coil impedance due to the changes in the permeability of YIG thin film during the excitation of magnetization dynamics.

III. Results and Discussion

Figure 1a shows the XRD pattern of GGG (001)/YIG sample recorded in lock-coupled mode for 2θ = 20° to 70° range. The presence of Bragg reflections corresponding to (004) and (008) YIG planes confirms the formation of epitaxial YIG (001) thin film without any additional phases. However, the observed two small additional peaks around 44° and 64° are from substrates holder, which is confirmed by performing the XRD scan after removing the

sample, while keeping all the conditions same. The magnified view around 2θ = 28.7° and 2θ = 59.5° in Figure 1b and 1c respectively unveiled the distinct appearance of characteristic YIG reflections observed together with the resolved $K_{\alpha 1}$ and $K_{\alpha 2}$ peaks for (004) and (008) GGG planes. To further access the epitaxy of YIG, cross-sectional TEM imaging is shown in Figure 1d. The thickness of the YIG thin film was found to be 45 nm. The lattice planes resolved TEM image, refer Figure 1e, across the interface of the GGG (001) substrate and YIG film confirms the epitaxial growth, consistent with the XRD results. An atomically sharp interface between the GGG and YIG is observed where very small lattice mismatch between YIG and GGG around ~0.05%, enables the favourable growth of epitaxial YIG thin film without any dislocations and distortions. The selected area electron diffraction along [100] zone axis, shown in Figure 1f, illustrates the anticipated cubic symmetry of highly crystalline and single-phase epitaxial YIG thin film.

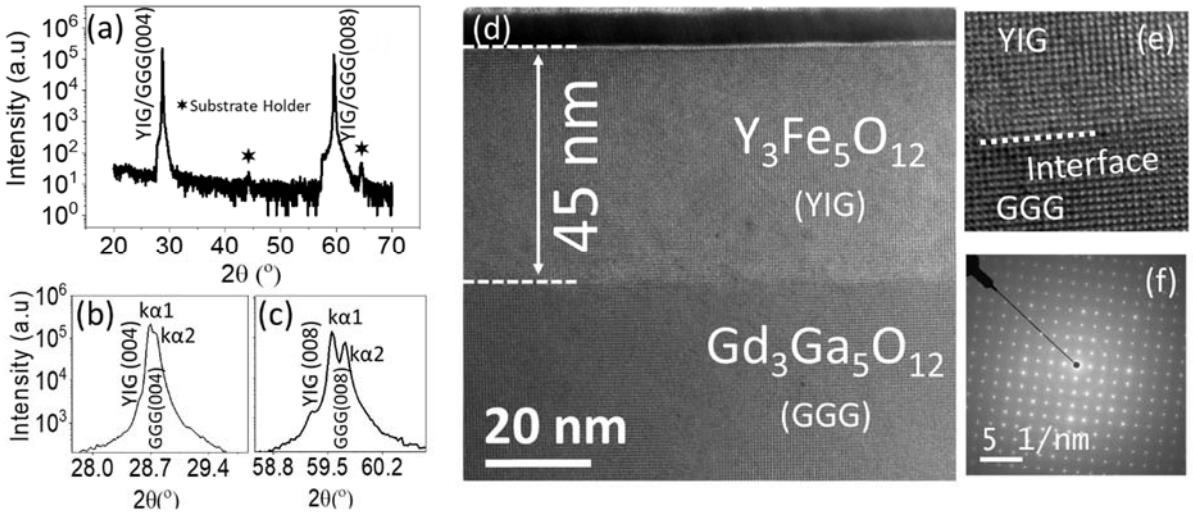

Figure 1. (a) XRD pattern of GGG(001)/YIG(001) sample recorded in lock-coupled mode. The magnified view showing (hkl) reflections for YIG (001) and resolved $K_{\alpha 1}/K_{\alpha 2}$ peaks of GGG (001) for (a) (004) peak and (b) (008) peak. (d) Cross-sectional TEM image of GGG(001)/YIG interface displaying epitaxial (001) growth. High-resolution TEM displaying atomically defined interface marked with white dotted line. (f) Selected area electron diffraction of YIG film describing high crystallinity with cubic phase.

The aberration-corrected (AC) - scanning transmission electron microscopy (STEM) image of the YIG thin film is shown in Figure 2a. The AC-STEM images are recorded using a

high angle annular dark field (HAADF) detector, which reflects image contrast according to atomic number (material density). Here the bright area corresponds to bottom GGG (001), and the darker area is showing grown YIG (001) thin film. Further the zoom view in inset verifies the perfectly epitaxial growth of YIG (001) along the z-axis with atomically resolved cubic lattice without any visible dislocations. In addition, distinct Kiessig fringes observed in XRR data (refer Fig 2b) for the YIG film provide a strong evidence of sharp interface and excellent surface quality of entire thin film. The interface roughness of GGG/YIG is estimated to be 0.13 nm by simulating the experimental data (open circles) as shown by overlapping spectra (red line) in Figure 2b assuming a bilayer model GGG/YIG. Next, the M-H hysteresis loops at different azimuthal angles (Θ) were traced by varying the external magnetic field (H_{DC}) direction (red arrow) with respect to YIG crystallographic [100] orientation (white arrow) as depicted in figure 2(c). Figure 2d shows azimuthal angular dependent M-H hysteresis loops that proves the in-plane easy axis and hard axis of the YIG is parallel to [100] (Θ=0°) and [110] (Θ=45°) orientation respectively. Moreover, the Θ dependence of coercive field plotted in Figure 2e clearly shows the in-plane biaxial anisotropy related to the cubic crystallographic four-fold symmetry. The coercive field of the YIG thin film along [100] and [110] is found to be ~ 1.9 Oe and 1.3 Oe respectively.

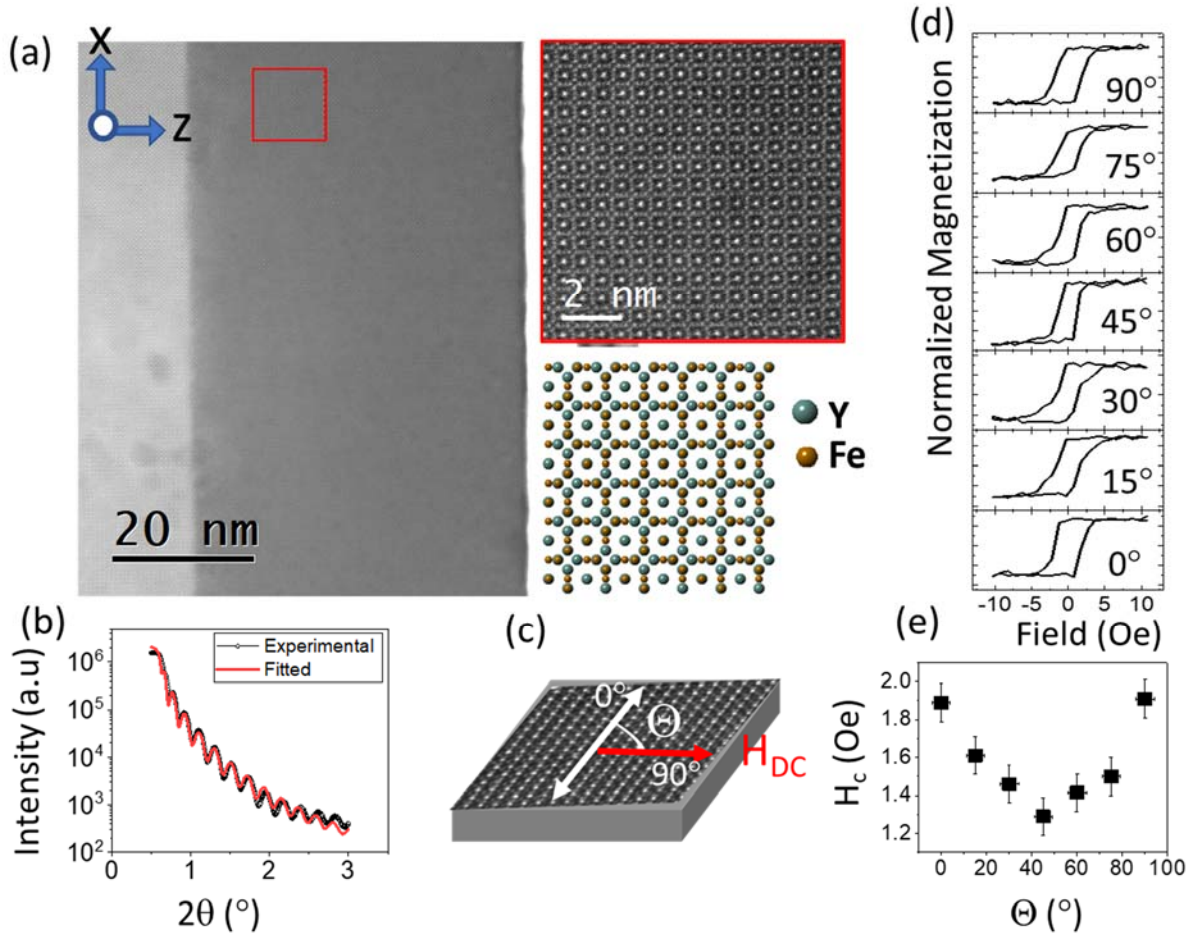

Figure 2. (a) Aberration corrected (AC)- Scanning Transmission Electron Microscopy (STEM) showing the cubic lattice of the 45 nm YIG (001) thin film. (b) X-ray reflectivity measurements of YIG (001)/GGG (001). (c) Schematic showing the in-plane angle (Θ) between the [100] and applied magnetic field. (d) M-H loop and (e) coercive field as a function of Θ.

MI measurements were performed to study low frequency magnetization dynamics of epitaxial YIG (001) thin film. Figure 3a shows cartoon representation of one-turn inductor made up of copper strip which was specifically designed to measure the impedance change during the dynamics. Upon passing I_{rf} current in this designed strip coil, the distribution and strength of generated rf magnetic field defined by Hx, Hy, and Hz along x, y and z direction respectively was also simulated using the RF module of COMSOL Multiphysics. The Hy is determined to be 0.13 Oe with negligible amplitude in x and z-direction. Further invariant

amplitude of all rf field components up to 2000 MHz as shown in Figure 3b, suggest the reliability of present MI measurements performed along different crystallographic directions of YIG, while sweeping the DC magnetic field (H_{DC}) along with different excitation rf magnetic field (H_{rf}). As mentioned before, the I_{rf} current passing through the copper strip coil creates an H_{rf} along the axial direction and therefore the sample GGG (001)/YIG placed in the strip coil will experience an in-plane H_{rf} magnetic field (refer Fig 3c). The angle between the H_{rf} and applied DC magnetic field (H_{DC}), with H_{DC} initially applied along [100] direction, is given by ϕ. Further, to understand the magnetization dynamics in the YIG, MI measurements were performed as a function of excitation frequency for a given direction of applied magnetic field i.e, ϕ=0° (for [100]) and ϕ=45° (for [110]). The angular dependent MI measurements are carried out by moving the electromagnets to vary azimuthal angle (ϕ) at 1000 MHz while varying in-plane H_{DC} as shown in Figure 3d. The similar value of the resonant fields along [110] (for ϕ = 45°) and [-1-10] (for ϕ = –45°) direction of YIG film (Figure 3e) which further support the observed crystallographic cubic four-fold symmetry from TEM results.

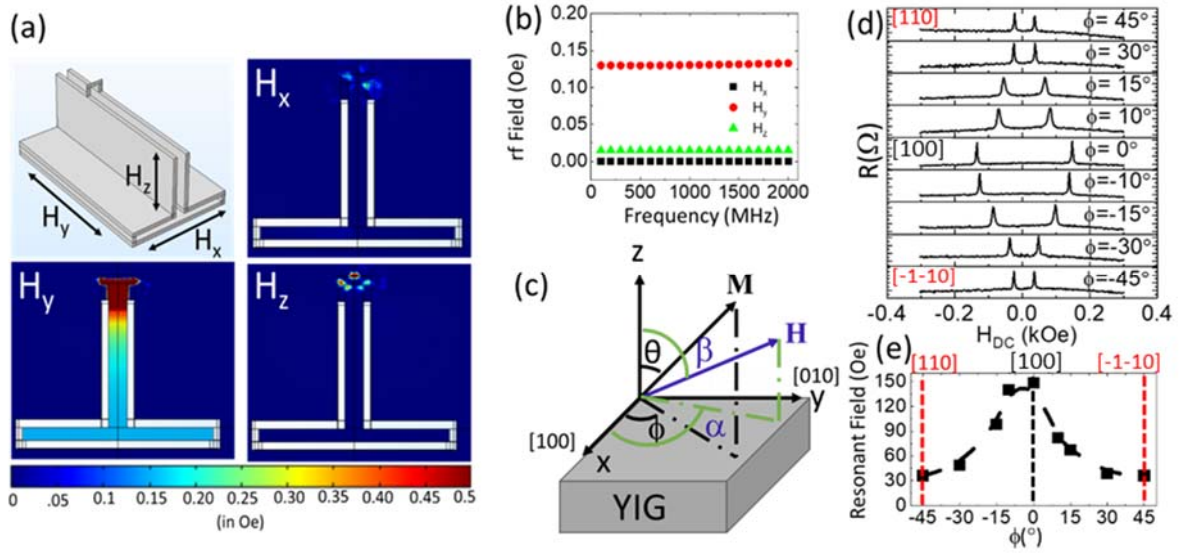

Figure 3. (a) Simulated RF magnetic field inside the copper strip coil along x, y and z directions using COMSOL simulation. (b) Estimated RF magnetic field as a function of excitation frequency. (c) Schematic showing the film is in x-y plane and the M and the H_{DC} make the elevation angles of θ and β with respect to the normal to the film plane respectively while their projections on the x-y (film) plane make the angles ϕ and α with respect to x-axis respectively. (d) The angular dependent MI measurements while varying the in-plane azimuthal angle ϕ at 1000 MHz. (d) Resonant field as a function of ϕ.

Figure 4a and 4b delineate the resonance field - frequency dispersion of GGG (001)/YIG sample recorded for ϕ=0° and ϕ=45°, respectively, over a frequency range of 500-2000 MHz, with in-plane magnetic field sweep. For ϕ=0°, two well-separated resonant peaks were observed in the low-frequency regime, up to 800 MHz, where the applied magnetic field is less than the saturation magnetic field (H_S) required for YIG. The peak observed at the lower magnetic field is marked as peak "p1" in Figure 4a. For excitation frequency, 900 MHz and above, the single resonance peak is observed confirming uniform Kittle excitation mode. However, for ϕ=45°, no resonant peak(s) were observed at lower frequencies up to 800 MHz, and only single resonant peaks were observed for all excitation frequencies above 800 MHz as shown in Figure 4b. The origin of the peak at lower applied magnetic fields (peak p1 in Figure 4a) in low-frequency range is due to the excitation of spin-dynamics when the magnetization vector of YIG is not aligned along the external field due to its magnetocrystalline anisotropy (MCA) field. As the applied magnetic field is increased, the external magnetic field overcomes the internal MCA field and results in a parallel alignment of magnetization with the external field. The resonance at higher fields corresponds to the ferromagnetic resonance where the magnetization direction of the YIG and the applied magnetic field are aligned. To check the effect of rf driving magnetic field on the resonant peaks below and above the anisotropy field, the power-dependent MI measurements at two distinct frequencies i.e, 800 MHz and 1000 MHz was performed, as shown in Figure 4c,d. Here we chose 800 MHz and 1000 MHz frequencies based on the excitation modes observed in Figure 4a. Notably, the power-dependent MI spectra

recorded for both frequency showed no change in the resonant field with excitation power, confirming the uniform magnetization precession in linear excitation regime.

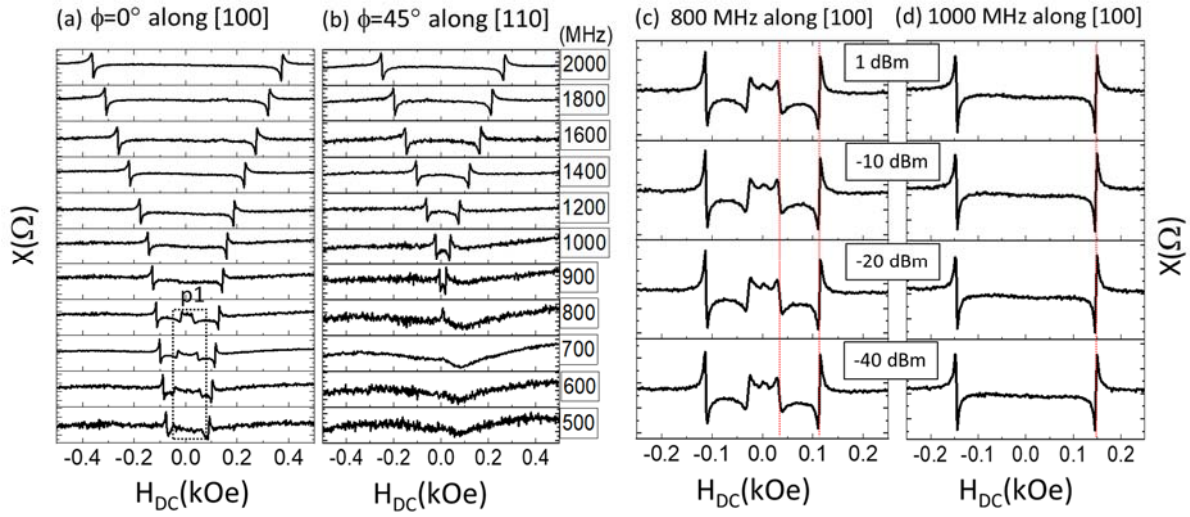

Figure 4. Impedance spectra of the copper strip coil for (a) ϕ=0° along [100] and (b) ϕ=45° along [110]. Power dependent magneto-impedance spectra of the copper strip coil for along YIG [100] direction at (c) 800 MHz and (d) 1000 MHz excitation frequencies.

The resonance field (H_R) and resonance linewidth (ΔH) are extracted by fitting MI spectra with the sum of the derivatives of antisymmetric Lorentzian function $X(H) = \sum_n \left(D \frac{\Delta H (H - H_R)}{(\Delta H)^2 + (H - H_R)^2} \right)$, where D is the intensity of the antisymmetric component[21]. The extracted H_R values are plotted against frequency for both ϕ=0° and ϕ=45° and are shown in Figure 5a by hollow blue squares and solid red circles, respectively. As expected, two distinct resonance peaks are observed for the low-frequency range from 500 to 800 MHz for ϕ=0°. However, above 800 MHz, a single resonance peak is observed for both the value of ϕ, i.e., ϕ=0° and ϕ=45°. In order to deduce cubic anisotropy field H_k, we solved the Smit-Beljers relation $\left(\frac{f}{\gamma}\right)^2 = [M_s \sin\theta]^{-2} \left(\frac{\partial^2 F}{\partial \theta^2} \frac{\partial^2 F}{\partial \phi^2} - \left(\frac{\partial^2 F}{\partial \theta \, \partial \phi} \right)^2 \right)$ [22], for magnetic free energy (F_{cubic}) expressed as the sum of the Zeeman, demagnetizing and cubic anisotropy energy terms given by

$$F_{cubic} = \frac{M_s}{2} [-2H(\sin\theta \sin\beta \cos(\alpha - \phi) + \cos\theta \cos\beta) + 4\pi M_s \cos^2\theta] + \frac{M_s}{2} H_k \cos^2\phi \sin^2\phi]$$

where M_s is the saturation magnetization, β and θ are the elevation angles of the external field and the magnetization respectively with respect to the normal of the film plane (as shown in Figure 3(c)), α and ϕ are the azimuthal angles of the external field and the magnetization respectively with respect to the x-axis on the film plane (refer Figure 3(c)). Thereby we can obtain the simplified expression; $\left(\frac{f}{\gamma}\right)^2 = (\mathrm{H}\cos(\alpha-\phi)+\mathrm{M_s})(\mathrm{H}\cos(\alpha-\phi)+\mathrm{H_k}\cos 4\phi)$, which shows a fourfold symmetry as is expected from cubic anisotropy fields. Here *f* is the excitation rf frequency and γ is the gyromagnetic ratio. At high fields where the magnetization direction of the ferromagnets and the applied magnetic field is parallel, i.e $(\alpha-\phi=0)$, this expression is reduced to $\left(\frac{\mathrm{f}}{\gamma}\right)^2 = (\mathrm{H}+\mathrm{M_s})(\mathrm{H}+\mathrm{H_k}\cos 4\phi)$.

Further, substituting the value of $\phi = 0°$ and $\phi = 45°$, we obtain the expressions $\left(\frac{\mathrm{f}}{\gamma}\right)^2 = (\mathrm{H}+\mathrm{M_s})(\mathrm{H}+\mathrm{H_{k,100}})$ and $\left(\frac{\mathrm{f}}{\gamma}\right)^2 = (\mathrm{H}+\mathrm{M_s})(\mathrm{H}-\mathrm{H_{k,110}})$ for [100] and [110] direction respectively on the film plane. The derived expressions were used to estimate the anisotropy fields $H_{k,100}$ and $H_{k,110}$ along [100] and [110] directions, respectively, by fitting the obtained resonance fields as a function of excitation frequencies as shown in Figure 5a. Fittings were performed by letting the gyromagnetic ratio and anisotropy fields as free parameters for the fixed value of M_s=1400 Oe. A similar value of anisotropy fields ~ ± 65 ± 2 Oe is found for both $H_{k,100}$ and $H_{k,110}$. The gyromagnetic ratios are found to be 2.739 MHz/Oe (for [100]) and 2.741 MHz/Oe (for [110]) which are in good agreement with fitting. For the case where magnetization is not parallel to the external magnetic field marked by dotted black box region in Figure 5a, we observe a decrease in the resonance frequency with increasing applied magnetic field. Such a decrease is because of the decrease in additional $(\alpha-\phi)$ term, as shown in the inset of Figure 5a, that is otherwise zero for high field regime. For the low field regime in $\phi = 45°$, we can obtain $\left(\frac{\mathrm{f}}{\gamma}\right)^2 = (\mathrm{H}\cos(45-\alpha)+\mathrm{M_s})(\mathrm{H}\cos(45-\alpha)-\mathrm{H_k})$. Assuming a

linear increase of α with increasing H_{DC}, we can fit the experimental data using this expression to a good level of accuracy. The corresponding fit is shown by the line in Figure 5a. Thus, the MI measurements provide a precise and effective way to investigate the magnetic properties such as anisotropy field, effective magnetization, of the magnetic material by exciting the magnetization dynamics. The method can be widely used for metal, semiconductors, and insulators[15-18, 23].

Subsequently, we plot the values of linewidth, ΔH, as a function of frequency when H_{DC} is along [100] and [110] as shown in Figure 5b. Along the [100] direction, when the $H_R > H_{k,100}$, an anticipated linear increase in the ΔH as a function of excitation frequency is observed. A low damping factor of $\alpha \sim 4.7 \times 10^{-4}$ is estimated by fitting the obtained ΔH as a function of frequency using the equation: $\Delta H = \Delta H_o + \frac{2\pi\alpha}{\gamma} f$ [21, 24]. However, at low frequency, when $H_R < H_{k,100}$, high values of ΔH are observed. The higher value of the observed ΔH is due to non-collinear precession below the anisotropy field, where the applied magnetic field and magnetization vector are not parallel to each other, shown in the inset of Figure 5a. This non-collinear precession of the magnetization is expected to provide the non-linear behaviour of the ΔH as a function of frequency below the anisotropy field as shown in the dotted red box in Figure 5b. A similar value of $\alpha \sim 6.1 \times 10^{-4}$ is also estimated when the magnetic field is applied in along the [110] direction. One order higher value of damping factor ~ 4.7-6.1×10^{-4} as compare to bulk YIG ~ 3×10^{-5} is observed. This ultralow value of Gilbert damping of 3×10^{-5} is possible in the fully relaxed thin film. The observed higher value of damping factor may also attribute to the presence of the extrinsic damping factors such as two-magnon scattering in the in-plane excitation geometry of epitaxial YIG thin films. The non-homogenous linewidth (ΔH_o) along the [100] and [110] is found to be 0.8 Oe and 0.6 Oe, respectively which confirms the good quality of the epitaxial thin film of YIG.

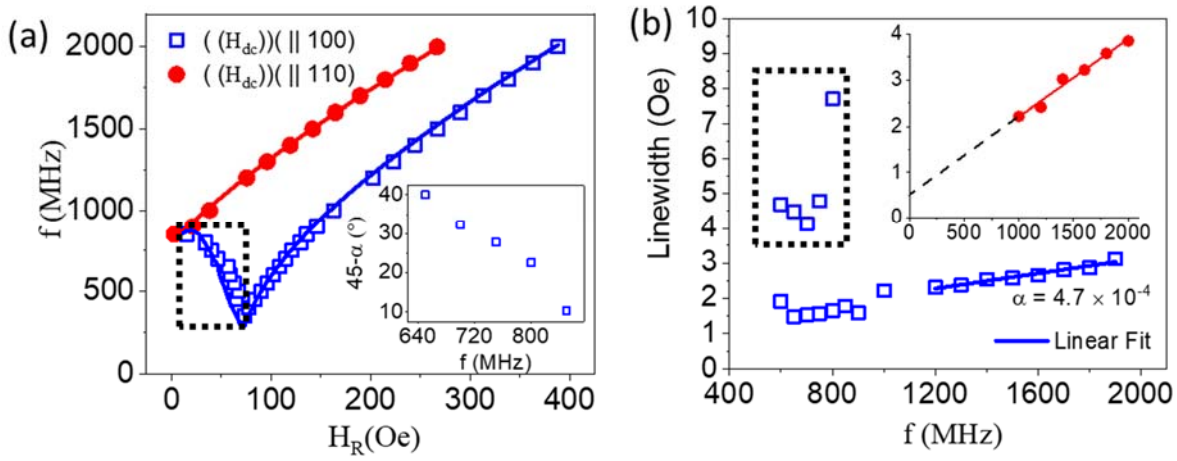

Figure 5. (a) Dispersion of resonance field with frequency when H_{dc} || [100] and H_{dc} || [110] direction. Inset shows the relative angle between the magnetization and applied magnetic field. (b) linewidth as a function of excitation frequency used to estimate the effective damping (α) for H_{dc} || [100] and H_{dc} || [110]. The x-y axis for inset and main Figure are the same. The black dotted box denoted the linewidth for the MI spectra below the anisotropy field.

Real ([R(Ω)]) and imaginary ([X(Ω)]) part of the MI spectra showing the two distinct resonant fields observed at 800 MHz excitation frequency is given in Figure 6 (top left). Careful analysis revealed that the X component changes its sign below the anisotropy field while the R component maintains the same sign. It is well established that the R component is directly proportional to the power absorbed by the sample through μ_r'', and hence R displays a positive peak at both the resonances. The opposite signs of X line shape differ significantly from the trend observed in μ_r' for the acoustic (AM) and optic mode (OM) in interlayer exchange coupled systems[25] . In this system, the sign of μ_r' remains the same for both AM and OM. Similarly, in inverse spin hall effect-spin pumping experiments, the FMR modes at below and above H_K show the same voltage sign[26]. Thus, the line shape of X gives additional spin information with regards to the magnetization which can be used to design magnonic devices.

It is important to note that the second resonance mode feature below the anisotropy fields are very sensitive to the frequency of excitation and direction of the applied magnetic field. In order to take a closer look at multiple resonant states and dominant anisotropy field resulting in it, MI measurements were performed as a function of azimuthal angle "ϕ". It is

worthwhile to note that the resonance field-frequency dispersion color map shown in Figure 6 (b-l) delineate the substantial change within $-10° \leq \phi \leq 10°$. A systematic change in the visible dichotomy, where resonant modes for $H_R < H_{k,100}$ and $H_R > H_{k,100}$ merges, is observed with different orientation of the applied magnetic field. The mode occurring for $H_R < H_{K,100}$ is known as a soft mode which occurs when the magnetization of YIG film is not aligned with the applied magnetic field. The behavior of these soft modes reveals important information regarding magnetization switching. The resulting disappearance of the resonant mode corresponds to the magnetic domains for a fixed value of excitation frequency. Thus, the azimuthal orientation of the magnetic field relative to the YIG [100] axis of the epitaxial YIG thin film, shows a sharp change in the magnetization dynamics. This provides us a better way to control the magneto-dynamics for low-frequency range and its implementation to estimate the anisotropy field, and related spin transport effects in the YIG and other ferromagnetic materials.

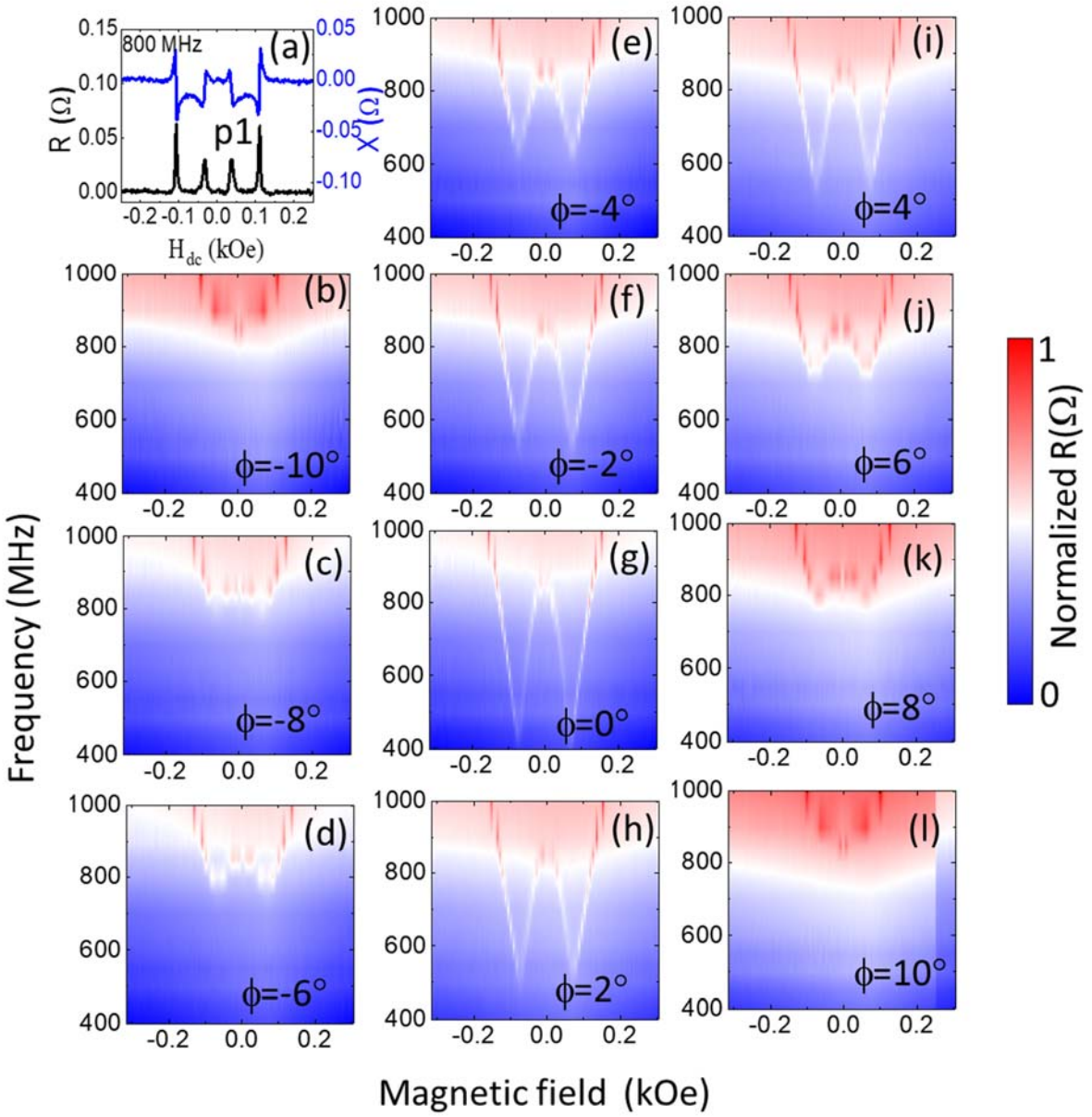

Figure 6. (a) Real and imaginary part of the MI spectra showing the two distinct resonant fields observed for 800 MHz excitation frequency. (b) to (l) resonance field-frequency dispersion color map for $-10° \leq \phi \leq 10°$ with the step size of 2° showing the change in the visible dichotomy with ϕ.

To conclude, we examine the magneto-dynamics of an epitaxial 45 nm YIG thin films using the magneto-impedance technique. A low value of the damping factor $\sim 4.7 - 6.1 \times 10^{-4}$ is estimated for the resonant field higher than the anisotropy field of ~ 65 Oe. The magneto-dynamics clearly shows the visible dichotomy between two resonant fields for $H_R < H_{k,100}$ and $H_R > H_{k,100}$ and its motion as a function of the direction of the applied magnetic field.

A good agreement between the analytic model fitting and the experimental data is demonstrated for both cases; (1) when the M is not parallel to the H_{DC} ($H_R < H_{k,100}$), and (2) when the M is parallel to the H_{DC} ($H_R > H_{k,100}$). Thus, the MI measurements provide a precise and effective way to investigate the magnetic properties such as anisotropy field, effective magnetization, gyromagnetic ratio, Gilbert damping of the magnetic material by measuring the impedance of the strip coil. Understanding the anisotropy field dependent resonance mode dispersions in the low-frequency mode could be helpful for designing the YIG based low-frequency resonators, oscillators, filters and magnonic devices[27-31]. The method can be widely used for metals, semiconductors and insulators.

Acknowledgment

This work was supported by the Ministry of Education (MOE) through grant number MOE2017-T2-2-129 and MOE2019-T2-1-058. R.M. also acknowledges the Ministry of Education, Singapore for supporting this work through grant No. MOE2016-T2-2-098. Y.F. acknowledges Japan Society for the Promotion of Science for supporting this work through grant No. 18H01862. M.D. acknowledges the financial support from Nanyang Technological University start-up grant M4081924. Transmission electron microscopy imaging was performed at the Facility for Analysis, Characterization, Testing and Simulation (FACTS) in Nanyang Technological University, Singapore.

References

(1) Zhou, H. G.; Fan, X. L.; Ma, L.; Zhang, Q. H.; Cui, L.; Zhou, S. M.; Gui, Y. S.; Hu, C. M.; Xue, D. S. Spatial symmetry of spin pumping and inverse spin Hall effect in the Pt/Y3Fe5O12 system. *Physical Review B* **2016,** *94* (13), DOI: 10.1103/PhysRevB.94.134421.

(2) Bartell, J. M.; Jermain, C. L.; Aradhya, S. V.; Brangham, J. T.; Yang, F. Y.; Ralph, D. C.; Fuchs, G. D. Imaging Magnetization Structure and Dynamics in Ultrathin Y3Fe5O12/Pt Bilayers with High Sensitivity Using the Time-Resolved Longitudinal Spin Seebeck Effect. *Physical Review Applied* **2017,** *7* (4), DOI: 10.1103/PhysRevApplied.7.044004.

(3) Du, C. H.; Wang, H. L.; Hammel, P. C.; Yang, F. Y. Y3Fe5O12 spin pumping for quantitative understanding of pure spin transport and spin Hall effect in a broad range of materials. *Journal of Applied Physics* **2015,** *117* (17), DOI: 10.1063/1.4913813.

(4) Oh, I.; Park, J.; Jo, J.; Jin, M. J.; Jang, M. S.; Lee, K. S.; Yoo, J. W. Solution-Processed Ferrimagnetic Insulator Thin Film for the Microelectronic Spin Seebeck Energy Conversion. *ACS Appl Mater Interfaces* **2018,** *10* (34), 28608-28614, DOI: 10.1021/acsami.8b08749.

(5) Zhang, D. N.; Jin, L. C.; Zhang, H. W.; Yang, Q. H.; Rao, Y. H.; Wen, Q. Y.; Zhou, T. C.; Liu, C.; Zhong, Z. Y.; Xiao, J. Q. Chemical epitaxial growth of nm-thick yttrium iron garnet films with low Gilbert damping. *Journal of Alloys and Compounds* **2017,** *695*, 2301-2305, DOI: 10.1016/j.jallcom.2016.11.089.

(6) Pati, S. P.; Endo, Y. Enhanced Low-Temperature Interfacial Gilbert Damping in Pt/YIG/Pt Trilayer Structures. *IEEE Transactions on Magnetics* **2019,** *55* (2), DOI: 10.1109/tmag.2018.2863678.

(7) Liang, X.; Zhu, Y.; Peng, B.; Deng, L.; Xie, J.; Lu, H.; Wu, M.; Bi, L. Influence of Interface Structure on Magnetic Proximity Effect in Pt/Y3Fe5O12 Heterostructures. *ACS Appl Mater Interfaces* **2016,** *8* (12), 8175-83, DOI: 10.1021/acsami.5b11173.

(8) Shang, T.; Zhan, Q. F.; Ma, L.; Yang, H. L.; Zuo, Z. H.; Xie, Y. L.; Li, H. H.; Liu, L. P.; Wang, B. M.; Wu, Y. H.; Zhang, S.; Li, R. W. Pure spin-Hall magnetoresistance in Rh/Y3Fe5O12 hybrid. *Sci Rep* **2015,** *5*, 17734, DOI: 10.1038/srep17734.

(9) Vélez, S.; Bedoya-Pinto, A.; Yan, W.; Hueso, L. E.; Casanova, F. Competing effects at Pt/YIG interfaces: Spin Hall magnetoresistance, magnon excitations, and magnetic frustration. *Physical Review B* **2016,** *94* (17), DOI: 10.1103/PhysRevB.94.174405.

(10) Sokolov, N. S.; Fedorov, V. V.; Korovin, A. M.; Suturin, S. M.; Baranov, D. A.; Gastev, S. V.; Krichevtsov, B. B.; Maksimova, K. Y.; Grunin, A. I.; Bursian, V. E.; Lutsev, L. V.; Tabuchi, M. Thin yttrium iron garnet films grown by pulsed laser deposition: Crystal structure, static, and dynamic magnetic properties. *Journal of Applied Physics* **2016,** *119* (2), DOI: 10.1063/1.4939678.

(11) Mohmed, F.; Dar, F. A.; Rubab, S.; Hussain, M.; Hua, L. Y. Magnetic and thermal properties of ferromagnetic insulator: Yttrium Iron Garnet. *Ceramics International* **2019,** *45* (2), 2418-2424, DOI: 10.1016/j.ceramint.2018.10.161.

(12) Lee, S.; Grudichak, S.; Sklenar, J.; Tsai, C. C.; Jang, M.; Yang, Q.; Zhang, H.; Ketterson, J. B. Ferromagnetic resonance of a YIG film in the low frequency regime. *Journal of Applied Physics* **2016,** *120* (3), DOI: 10.1063/1.4956435.

(13) Farle, M. Ferromagnetic resonance of ultrathin metallic layers. *Reports on Progress in Physics* **1998,** *61* (7), 755-826, DOI: 10.1088/0034-4885/61/7/001.

(14) Zakeri, K.; Lindner, J.; Barsukov, I.; Meckenstock, R.; Farle, M.; von Hörsten, U.; Wende, H.; Keune, W.; Rocker, J.; Kalarickal, S. S.; Lenz, K.; Kuch, W.; Baberschke, K.; Frait, Z. Spin dynamics in ferromagnets: Gilbert damping and two-magnon scattering. *Physical Review B* **2007,** *76* (10), DOI: 10.1103/PhysRevB.76.104416.

(15) Chaudhuri, U.; Mahendiran, R. Magnetoimpedance Response of a Double-Exchange Metallic Ferromagnet La0.80Sr0.20MnO3. *IEEE Transactions on Magnetics* **2019**, 1-5, DOI: 10.1109/tmag.2019.2902655.

(16) Lotze, J.; Huebl, H.; Gross, R.; Goennenwein, S. T. B. Spin Hall magnetoimpedance. *Physical Review B* **2014,** ٩(17), DOI: 10.1103/PhysRevB.90.174419.

(17) Chaudhuri, U.; Kumari, M.; Mahendiran, R. Indirect Permeability Measurements Using a "Strip Coil" for Co0.6Zn0.4Fe1.7Mn0.3O4. *IEEE Transactions on Magnetics* **2018,** *54* (11), 1-4, DOI: 10.1109/tmag.2018.2841995.

(18) Correa, M. A.; Rosa, W. O.; Melo, A. S.; Silva, E. F.; Della Pace, R. D.; Oliveira, A. B.; Chesman, C.; Bohn, F.; Sommer, R. L. Magnetoimpedance effect in ferrimagnetic insulator yttrium iron garnet films capped by copper. *Journal of Magnetism and Magnetic Materials* **2019,** *480*, 6-10, DOI: 10.1016/j.jmmm.2019.02.051.

(19) Santos, J. G. S.; Silva, E. F.; Rosa, W. O.; Bohn, F.; Correa, M. A. Role of the spin-orbit coupling on the effective damping parameter in Y3Fe5O12/(Ag,W) bilayers explored through magnetoimpedance effect. *Materials Letters* **2019,** *256*, DOI: 10.1016/j.matlet.2019.126662.

(20) Schaffer, M.; Schaffer, B.; Ramasse, Q. Sample preparation for atomic-resolution STEM at low voltages by FIB. *Ultramicroscopy* **2012,** *114*, 62-71, DOI: 10.1016/j.ultramic.2012.01.005.

(21) Medwal, R.; Gupta, S.; Rawat, R. S.; Subramanian, A.; Fukuma, Y. Spin Pumping in Asymmetric Fe50Pt50/Cu/Fe20Ni80Trilayer Structure. *physica status solidi (RRL) – Rapid Research Letters* **2019,** *13* (10), DOI: 10.1002/pssr.201900267.

(22) Smith, J.; Bejlers, H. G. Ferromagnetic resonance absorption in BaFe12O19, a high anisotropy crystal. *Philips Res. Rep.* **1955,** *10*.

(23) Kumar, A.; Mohapatra, S.; Fal-Miyar, V.; Cerdeira, A.; García, J. A.; Srikanth, H.; Gass, J.; Kurlyandskaya, G. V. Magnetoimpedance biosensor for Fe3O4 nanoparticle intracellular uptakeevaluation. *Applied Physics Letters* **2007,** *91* (14), DOI: 10.1063/1.2790370.

(24) Gupta, S.; Medwal, R.; Kodama, D.; Kondou, K.; Otani, Y.; Fukuma, Y. Important role of magnetization precession angle measurement in inverse spin Hall effect induced by spin pumping. *Applied Physics Letters* **2017,** *110* (2), DOI: 10.1063/1.4973704.

(25) Li, S.; Wang, C.; Chu, X. M.; Miao, G. X.; Xue, Q.; Zou, W.; Liu, M.; Xu, J.; Li, Q.; Dai, Y.; Yan, S.; Kang, S.; Long, Y.; Lu, Y. Engineering optical mode ferromagnetic resonance in FeCoB films with ultrathin Ru insertion. *Sci Rep* **2016,** *6*, 33349, DOI: 10.1038/srep33349.

(26) Papaioannou, E. T.; Fuhrmann, P.; Jungfleisch, M. B.; Bracher, T.; Pirro, P.; Lauer, V.; Losch, J.; Hillebrands, B. Optimizing the spin-pumping induced inverse spin Hall voltage by crystal growth in Fe/Pt bilayers. *Applied Physics Letters* **2013,** *103* (16), DOI: Artn 16240110.1063/1.4825167.

(27) Zhang, Z. Z.; Liu, J. L.; Ding, H.; Feng, Z. K.; Nie, Y. Microwave Bandpass Filters Tuned by the Magnetization of Ferrite Substrates. *Ieee Magnetics Letters* **2017,** *8*, DOI: 10.1109/lmag.2016.2623717.

(28) Wang, J. W.; Geiler, A.; Mistry, P.; Kaeli, D. R.; Harris, V. G.; Vittoria, C. Design and simulation of self-biased circulators in the ultra high frequency band. *Journal of Magnetism and Magnetic Materials* **2012,** *324* (6), 991-994, DOI: 10.1016/j.jmmm.2011.10.006.

(29) Firby, C. J.; Elezzabi, A. Y. Design of integrated YIG-based isolators and high-speed modulators. *Ultrafast Phenomena and Nanophotonics Xx*; Betz, M.; Elezzabi, A. Y., Eds.; 2016.

(30) Bhoi, B.; Cliff, T.; Maksymov, I. S.; Kostylev, M.; Aiyar, R.; Venkataramani, N.; Prasad, S.; Stamps, R. L. Study of photon-magnon coupling in a YIG-film split-ring resonant system. *Journal of Applied Physics* **2014,** *116* (24), DOI: 10.1063/1.4904857.

(31) Papa, E.; Barnes, S. E.; Ansermet, J. P. Local Excitation of Magnetostatic Modes in YIG. *IEEE Transactions on Magnetics* **2013,** *49* (3), 1055-1059, DOI: 10.1109/tmag.2012.2229386.